JACS
JOURNAL OF THE AMERICAN CHEMICAL SOCIETY
pubs.acs.org/JACS
Article

Strain-Modulated Seeded Growth of Highly Branched Black Au Superparticles for Efficient Photothermal Conversion

Qixuan Zhong, Ji Feng, Bo Jiang,* Yulong Fan, Qiao Zhang, Jinxing Chen,* and Yadong Yin*

Cite This: J. Am. Chem. Soc. 2021, 143, 20513−20523

ABSTRACT: Creating highly branched plasmonic superparticles can effectively induce broadband light absorption and convert light to heat regardless of the light wavelength, angle, and polarization. However, their direct synthesis in a controllable manner remains a significant challenge. In this work, we propose a strain modulation strategy to produce branched Au nanostructures that promotes the growth of Au on Au seeds in the Volmer−Weber (island) mode instead of the typical Frank−van der Merwe (layer-by-layer) mode. The key to this strategy is to continuously deposit polydopamine formed *in situ* on the growing surface of the seeds to increase the chemical potential of the subsequent deposition of Au, thus achieving continuous heterogeneous nucleation and growth. The branched Au superparticles exhibit a photothermal conversion efficiency of 91.0% thanks to their small scattering cross-section and direction-independent absorption. Even at a low light power of 0.5 W/cm^2 and a low dosage of 25 ppm, these particles show an excellent efficacy in photothermal cancer therapy. This work provides the fundamental basis for designing branched plasmonic nanostructures and expands the application scope of the plasmonic photothermal effect.

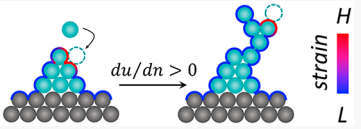

INTRODUCTION

Plasmonic superparticles with three-dimensional (3D) branched nanostructures feature blackbody-like absorption that can capture and convert all radiation to heat regardless of wavelength, angle, and polarization.[1−4] They hold great promise in laser (polarized light)-related photothermal applications, such as photothermal cancer therapy.[5−9] In comparison, the 1D and 2D nanostructures have lost absorption due to their polarization-dependent resonance (see more a detailed discussion in part I of the Supporting Information).[10,11] Another incentive for using 3D branched plasmonic superparticles is their small scattering cross-sections, which result in high absorption efficiency conducive to photothermal conversion since absorption efficiency is equal to $\frac{\sigma_{abs}}{\sigma_{abs}+\sigma_{sca}} = \frac{\sigma_{abs}}{\sigma_{ext}}$, where σ_{abs}, σ_{sca}, and σ_{ext} stand for absorption, scattering, and extinction cross-sections of the nanoparticles, respectively.[12,13] Conversely, the absorption and scattering cross-sections of 1D and 2D plasmonic nanostructures reach maximum values simultaneously at their resonant frequencies, causing a large amount of light to scatter out of the plasmonic heating system.[14,15] As a result, the photothermal conversion efficiencies (PCEs) of reported conventional plasmonic nanostructures (<50%) are usually much lower than the theoretical ones (>90%).[16,17]

Despite the promising application prospects of 3D branched plasmonic superparticles, their synthetic methods are still limited to selective etching (top-down) and self-assembly (bottom-up) strategies. Selective leaching of the less-stable M components (e.g., Ag or Cu) from Au−M alloyed nanoparticles was found to form 3D porous Au nanofoams with broadband absorption.[18,19] However, it requires complex fabrication procedures, typically including bimetallic nanostructure formation, alloying, and dealloying processes, therefore inevitably wasting precious metals. On the other hand, the self-assembly method can cluster building blocks (small Au nanoparticles) into superstructures with broadband absorption,[1,8,20] but their structures are bonded by noncovalent interactions that are sensitive to the surroundings, such as changes in temperature, pH, and ionic strength. Moreover, the assembled colloidosomes typically have large sizes (>200 nm), which are not suitable for many applications such as *in vivo* therapy. Direct chemical synthesis represents the most straightforward way to produce nanostructured materials. In particular, polymeric ligands have been explored for modulating the syntheses of nanocrystals with different dimensions in the past few years, with many examples demonstrated by Lin et al. in the synthesis of nanocrystals of various morphologies and surface properties using nonlinear block copolymer as ligands.[21,22] However, the effectiveness of using polymeric ligands in creating branched Au superparticles has not been demonstrated.[23,24]

Here, we propose using *in situ* polydopamine deposition to modulate the surface strain of growing seeds to directly synthesize highly branched Au superparticles. The key to this synthetic scheme is that the adsorption of polydopamine

Received: October 24, 2021
Published: November 23, 2021

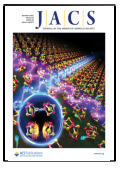

https://doi.org/10.1021/jacs.1c11242
J. Am. Chem. Soc. 2021, 143, 20513−20523

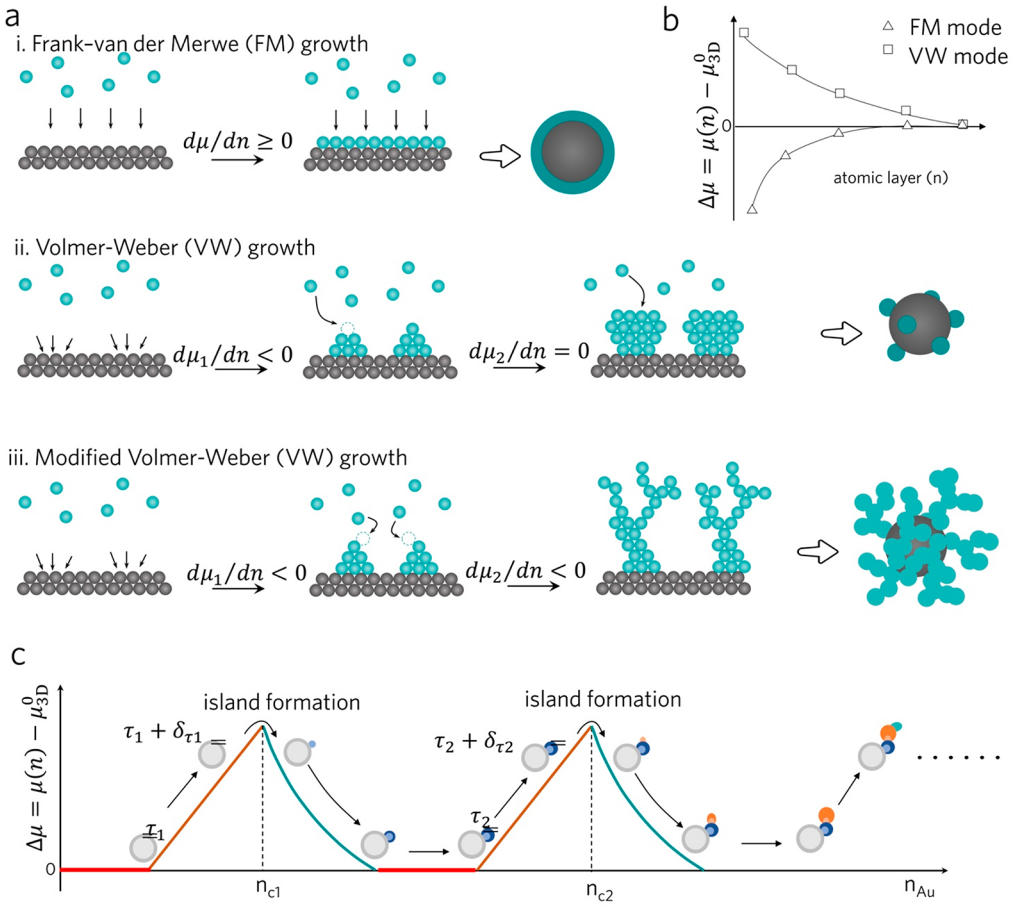

Figure 1. Morphological modulation in the seeded growth process. (a) Schematic illustration of crystal growth modes, including Frank−van der Merwe, Volmer−Weber, and modified Volmer−Weber modes. (b) Schematic dependence of the nanoparticle chemical potential on the atomic deposition thickness for the two Frank−van der Merwe and Volmer−Weber growth modes. (c) Chemical potential change of the layer-by-layer growth (red line) and island growth (brown and cyan curves) as functions of the amount of Au deposited on the seeds, n_{Au}.

constantly renews the surface property of the Au seeds to ensure continuous island growth on previously grown Au islands. Different from the conventional cases where the large chemical potential due to polymer adsorption is reduced for the successively grown islands, the *in situ* formed polydopamine strongly binds to the newly formed Au islands as the reaction progresses, enabling the island-on-island growth of the Au nanostructures. Importantly, the as-formed 3D highly branched Au nanostructures exhibit a broadband absorption and an extraordinary photothermal conversion efficiency of 91.0%, which is attributed to both the large absorption/extinction ratio and polarization independence. Their superior photothermal efficiency allows us to further demonstrate the efficacy of these branched Au superparticles in cancer therapy and reveal their detailed biomolecular mechanism by proteomic analysis.

RESULTS AND DISCUSSION

Theoretical Analysis of the Seed-Mediated Growth Mode. The growth mode of newly formed atoms (a) on the surface of a metallic seed (b) depends critically on the interfacial bonding strength of a and b and the bonding strength with the same crystal a. A model for describing the chemical potential per atom in the first several monolayers has been proposed as follows:[25,26]

$$\mu(n) = \mu^0_{3D} + [E_{aa} - E_{ab}(n)] \quad (1)$$

where μ^0_{3D} is the bulk chemical potential of the core material and E_{aa} and E_{ab} are the interatomic energies per atom needed to disjoin a half-crystal a from a half-crystal a and a half-crystal b, respectively. For specific a and b, μ^0_{3D} and E_{aa} are fixed. The term E_{ab} is determined by the desorption energy of a from b and the strain energy, both of which are related to the number of atomic layers (n) of a. Weak interaction and a large mismatch between a and b indicate a value of μ higher than μ^0_{3D}, resulting in the formation of a islands on b. As the deposition of a continues, the value of $\mu(n)$ decreases and approaches μ^0_{3D}. The criterion for a seeded growth mode depends on the first derivative of the chemical potential with respect to the number of atomic layers ($d\mu/dn$). When $d\mu/dn \geq 0$, the deposition of the next layer of a has a higher chemical potential than the current layer. The deposition prefers finishing the current layer first, resulting in a layer-by-layer growth mode (Frank−van der Merwe (FM) growth, Figure 1a-i and b). On the other hand, when $d\mu/dn < 0$, the growth follows the Volmer−Weber (VW) growth mode, forming islands on the pre-existing surface (Figure 1a-ii and b).

The formation of highly branched 3D nanostructures from seeds requires continuous island growth. However, due to the matched crystal structure, the growth of Au on the Au seed usually follows the FM mode, yielding crystals of increasing sizes. Premodification of the seed surface with ligands and

https://doi.org/10.1021/jacs.1c11242
J. Am. Chem. Soc. 2021, 143, 20513−20523

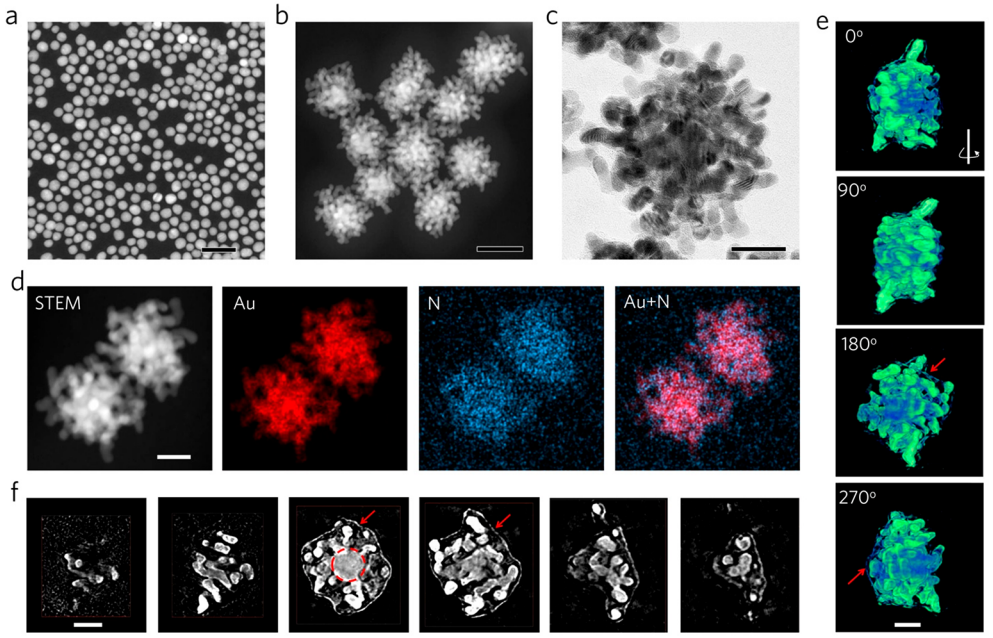

Figure 2. Structural characterizations of Au nanostructures. STEM images of (a)Au seeds and (b) Au nanostructures. (c) TEM image of Au nanostructures. (d) HAADF-STEM and elemental mapping images showing the elemental distribution of Au and N and the overlap. (e) Reconstructed 3D images of Au nanostructures at different rotation angles (0°, 90°, 180°, and 270°). (f) Ortho-slices of the reconstructed structure in panel e, where the step depth is 9 nm. Scale bars in panels a and b are both 50 nm, and those in panels c–f are all 20 nm.

mismatched metals may increase the surface energy, thus realizing the transformation of the growth mode from FM to VW ($d\mu_1/dn < 0$).[27,28] However, island growth does not guarantee the formation of highly branched 3D Au superstructures, since the growth mode would switch back to the FM mode after the deposition of a few layers of Au on the seed surface ($d\mu_2/dn = 0$). As a result, only some simple structures that do not exhibit blackbody-like absorption behavior, such as core–satellite structures and interfaced nano-oligomers, are obtained (Figure 1a-ii).[29]

To promote continuous island growth, we employ a polymer to modify the surface of the seed and renew the chemical nature of the newly formed surface during the seeded growth. This strategy continuously modifies E_{ab}, preventing the value of μ from approaching μ_{3D}^0 and leading to a continuously updated $d\mu_2/dn$. As a result, 3D structures are formed (Figure 1a-iii). The changes in the chemical potential related to the morphological evolution can be explained by a simple thermodynamic model, which is depicted in Figure 1c. In this case, the deposition of Au atoms on a Au seed is driven by the difference between μ_{NP} and $\mu_{solution}$. In the initial stage of the reaction, the adsorption of polymer on the Au seed surface is small, and the change of the surface energy of the seed is insubstantial. The growth follows the FM mode, increasing only in size (red line in Figure 1c, $\Delta\mu = 0$). As the amount of the adsorbed polydopamine increases, the system becomes complicated. The change in the chemical potential $\Delta\mu$ is a function of core radius (r) and the amount of deposited Au (n_{Au}) (see part II in the Supporting Information) as follows:[30]

$$\Delta\mu(r, n_{Au}) = \left[\left(\frac{E_{shell}}{1-\nu_{shell}}\right) + \left(\frac{1-2\nu_{seed}}{E_{seed}}\right)\cdot\left(\frac{E_{shell}}{1-\nu_{shell}}\right)^2 \cdot \frac{n_{Au}}{\pi r^3}\right]\cdot(\varepsilon_{shell})^2 \cdot V_m \quad (2)$$

where E_i, ε_i, and ν_i are the Young's modulus, Poisson's ratio, and lattice strain, respectively; r is the radius of the seed nanoparticle; and V_m is the standard molar volume of a Au atom. Obviously, the chemical potential of the nanoparticle increases with ν_{shell}, which is caused by the absorbed polymer chains. As a result, μ_{NP} will quickly accumulate to a critical value, thus forming a new island. The heterogeneous nucleation would rapidly release the accumulated energy, and the subsequent growth would switch back to the fresh surface, following the FM mode. By repeating the above processes, highly branched Au nanostructures can be obtained. Notably, the above discussion does not include the size effect following the Gibbs–Thomson relation ($\Delta\mu = 2\gamma V_m/r$, where γ, V_m, and $1/r$ are the surface energy, the molar volume, and the surface curvature of the nanoparticles, respectively).

Synthesis and Characterization of Branched Au Superparticles. The theoretical understanding paves the way for the design and preparation of branched Au superparticles. The traditional growth regulation approaches rely on the selective adsorption of ligand (CTA^+) or metal ions (Ag^+) on the crystal surface to guide the deposition of newly generated Au atoms,[31] which strongly depends on the seeds' crystal structures. Moreover, nanoparticles have a limited growth period, which is significantly reduced when the entire surface of the nanoparticles is covered in ligands such as CTAB. Here, we propose using polydopamine, which is produced simultaneously when the gold precursor is reduced, to regulate the crystal growth. It ensures continuous island growth on previously grown Au islands, forming hyperbranched structures. First, PVP-capped Au nanoparticles with an average size of ~14 nm (Figure 2a) were synthesized as seeds for the subsequent overgrowth. The Au seeds were then mixed with a Tri-HCl buffer solution (pH 8.5, 10 mM), dopamine, and $HAuCl_4$. The mixture was stirred for 6 h under flowing N_2 to obtain the final multibranched 3D Au superparticles with a black color (Au, Figure 2b and c). The energy-dispersive X-ray spectrometry (EDS) maps(Figure 2d, S2) show that the distribution of nitrogen is slightly broader

https://doi.org/10.1021/jacs.1c11242
J. Am. Chem. Soc. 2021, 143, 20513–20523

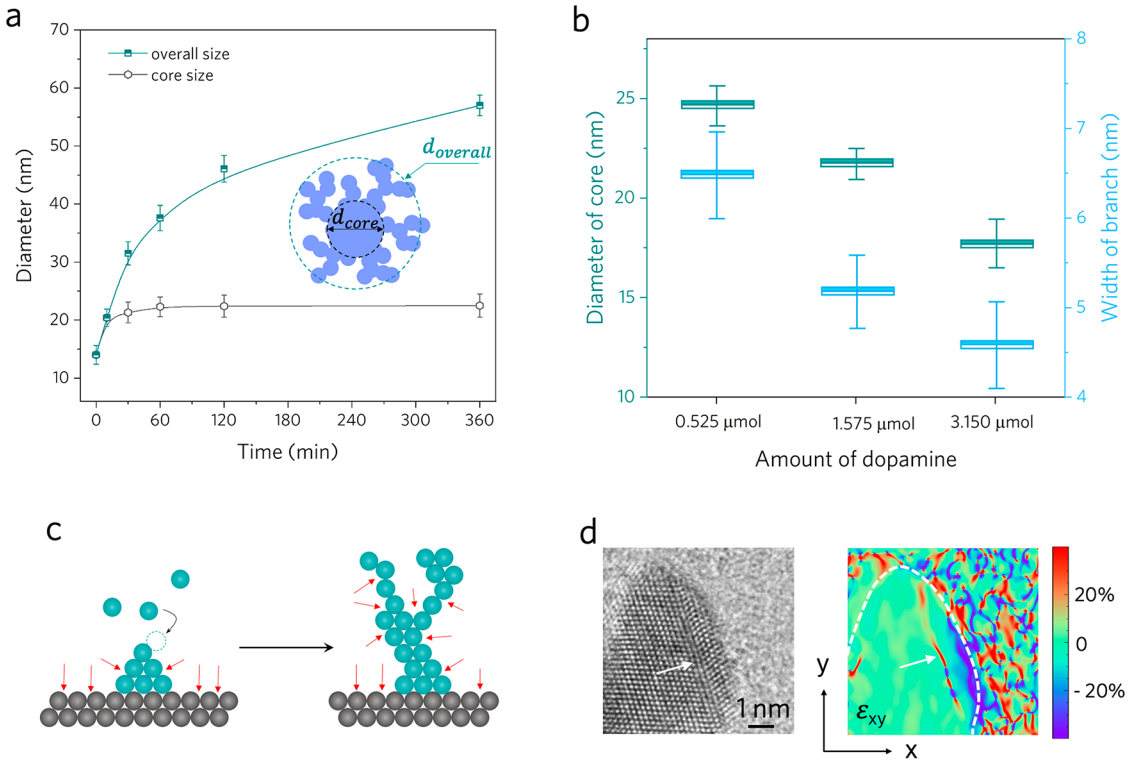

Figure 3. Mechanism investigation of seed-mediated island growth. (a) The overall and core size statistics of Au nanostructures versus the reaction time. The statistics were recorded by randomly counting 100 individual particles. (b) The average sizes of the cores and widths of the branches of Au nanostructures versus the amount of dopamine. (c) Schematic illustration of impact of the confinement effect on the growth of Au branches by polydopamine. (d) HRTEM image and corresponding strain distributions of the shear component (ε_{xy}) determined by a geometric phase analysis.

than that of Au, which is attributed to surface-covered polydopamine. Notably, dopamine has a weak reducibility and a strong coordinative capability, which dramatically reduces the reaction rate to favor the island growth. The sizes of the branched Au nanostructures could be precisely controlled from 57.6 to 124.2 nm after different growth generations (Figure S3), meeting the size requirements of various potential applications.

The fine structure of one typical Au was analyzed with electron tomography by rotating the sample from −70° to 70° with a 1° interval on a TEM grid (supplementary video 1). No noticeable mass loss or radiation damage was observed during the data acquisition process. By reconstructing (Figure 2e and supplementary video 2) and slicing (Figure 2f and supplementary video 3) the multiple sets of the obtained pictures, we can clearly see that the branches are uniformly distributed around the core (highlighted by the red dot ring in Figure 2f) and tightly wrapped by polydopamine (indicated by red arrows). In combination with TEM images at typical rotation angles (Figure S4), the tomographic results confirm that Au nanostructures have a 3D branched morphology, which may help eliminate the polarization deficiency.

Structural Evolution. The successful synthesis of branched Au superparticles encourages a further exploration of the growth process. The Au nanoparticles were isolated from the solution at different reaction stages by centrifugation and carefully characterized. After 5 min of reaction, the average size of the cores increased to 18.6 nm, but no obvious island was observed. When the reaction has progressed to 10 min, the size of the Au core increased to 20.4 nm, and some small Au islands emerged on the core surface, indicating a pronounced VW growth mode (Figure S5). Subsequent growth led to the formation of multibranch structures with a significantly larger overall size (Figure 3a), while the cores showed a negligible size change in the later period.

We divide the growth of Au into two stages. In the first 10 min of the reaction, the increase in the core sizes indicates the conformal coating (FM mode) of Au. At this stage, the degree of polymerization of dopamine is low so that it does not significantly affect the growth mode of the Au. The polydopamine chains keep growing until reaching their solubility limit in the solution, determined by the critical precipitation molecular weight, Mn_c.[32] Before the polydopamine grows sufficiently large to reach Mn_c, the deposition of Au atoms on the surface of the seeds mainly follows the FM growth mode. After reaching Mn_c, however, polydopamine precipitates from the solution and predominately covers the Au surface, increasing the chemical potential for further Au deposition and switching the growth mode to the VW mode. The above understanding was proven by adjusting the dopamine polymerization rate and comparing the sizes of the Au cores. Figures 3b and S6 show a decrease in the core size with the addition of more dopamine due to the reduced time required to form polydopamine precipitates. In addition, an increase in the concentration of dopamine also limited the conformal coverage of the islands (Figures 3b and c and S6), and guaranteed the formation of highly branched structures. In addition, we also designed an experiment to delay the precipitation of polydopamine by adding dimethyl sulfoxide (DMSO), a good solvent for polydopamine. When 200 μL of DMSO was added into the reaction system, the core size of the final products could increase to 26 nm, indicating a longer layer-by-layer growth period (Figure S7a). Increasing the amount of DMSO to 1 mL caused the morphology of the

https://doi.org/10.1021/jacs.1c11242
J. Am. Chem. Soc. 2021, 143, 20513−20523

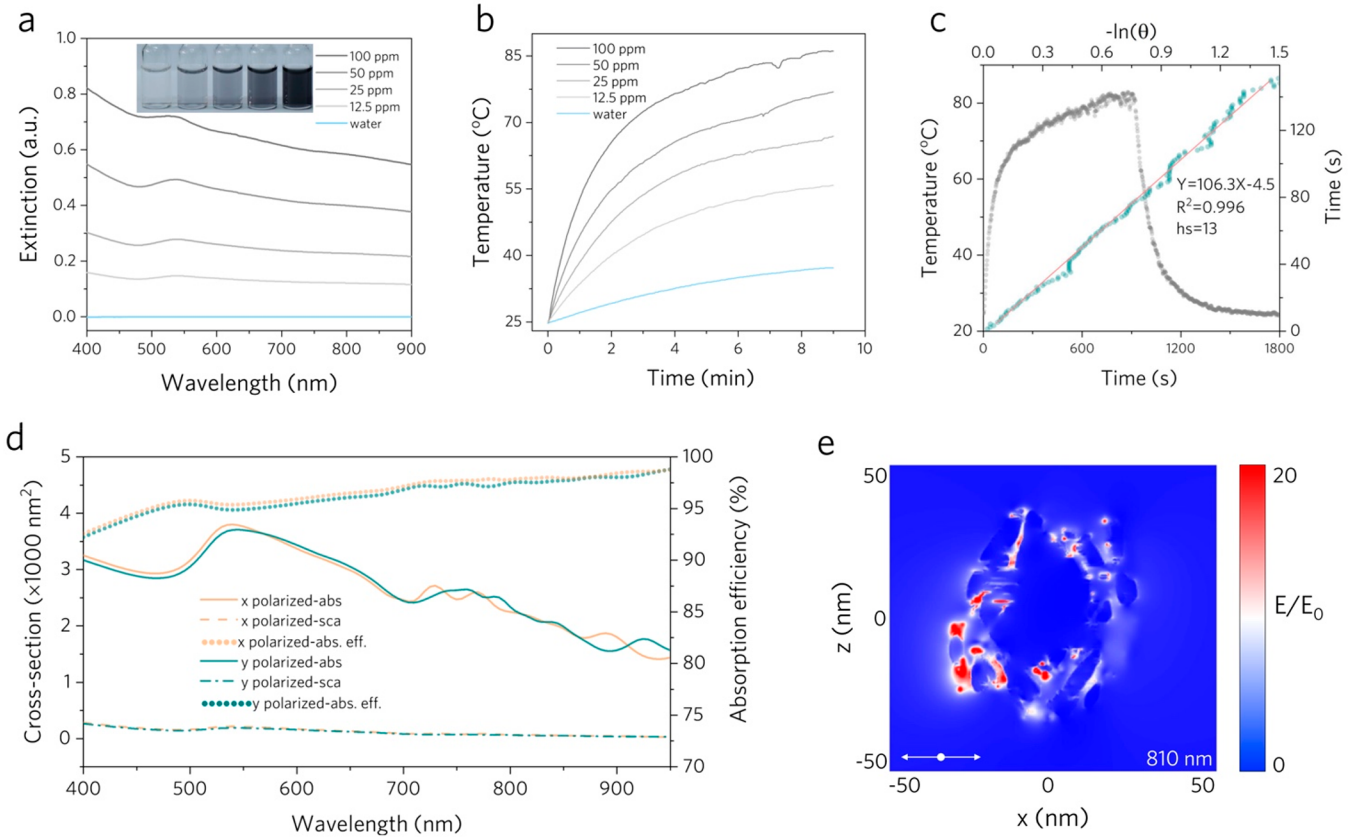

Figure 4. Light-to-heat conversion ability of branched Au superparticles. (a) UV−vis−NIR spectra of Au dispersions with different concentrations of 0, 12.5, 25, 50, and 100 ppm. The inset is the corresponding photograph from left to right. (b) Temperature curves of Au dispersions with different concentrations under 808 nm laser irradiation (1.0 W/m^2). (c) Calculation of the photothermal conversion efficiency at 808 nm. Gray dots show the photothermal effect of an aqueous dispersion of Au under irradiation with a laser for certain periods, then the laser was switched off. Green dots show the time constant (τ_s) for the heat transfer from the system determined by applying the linear time data from the cooling period. (d) Simulated absorption and scattering cross-sections and calculated absorption efficiency for the Au sample with different polarization directions. (e) Electric near-field enhancement distribution in the Au superparticles at 810 nm.

product to change from hyperbranched structures to small islands, and the size of the core also increased to 30 nm (Figure S7b). This result clearly shows that the precipitation of polydopamine and its subsequent adsorption on the surface of the seeds are important for regulating the growth mode.

We further reveal the key role of dopamine in this reaction as a reducing agent and a ligand precursor. First, dopamine has a catechol structure, which can quickly and strongly bind to newly formed crystal surfaces during growth.[33−35] As a result, the chemical potential of the seeds' surface increases significantly, which changes the deposition mode of Au atoms on Au seeds from layer-by-layer to continuous island growth. In this context, we used the same amount of catechol to mimic the role of dopamine, resulting in Au nanoparticles with rough surface structures (Figure S8). While the nonconformal coating of Au is consistent with our understanding of the strong affinity of this capping ligand for the Au surface, the absence of multibranched structures indicates its insufficient binding to the newly formed islands. Like most small-molecule ligands, their binding to the metal surface is dynamic,[36] allowing local epitaxial growth. In addition to the strong coordination of its catechol and amine groups to the Au surface, dopamine cross-links during polymerization. While reducing the gold precursor to drive growth on the seeds, dopamine itself is cross-linked simultaneously, forming a robust ligand film that prevents the newly formed islands from growing in a layer-by-layer manner.[37,38] The cross-linked structure of polydopamine in this work was also confirmed by dispersing Au superparticles in dimethylformamide (DMF). The presence of a lighter layer in the bright-field TEM image and a nitrogen signal in the EDS mapping image both prove that the polydopamine can not be dissolved by DMF, which is consistent with its cross-linked chemical structures (Figure S9). Such a cross-linked structure minimizes the dynamic nature of small capping ligands, providing a strong capping effect to modulate the surface strain and promote the island growth of Au on Au seeds.[39,40] In addition, we also used linear polyvinylpyrrolidone and polyallylamine as reference ligands. When the polyvinylpyrrolidone was used as the ligand, only quasi-spherical particles (~55 nm) were obtained (Figure S10) due to its relatively weak binding to the surface. With the stronger binding ability of the amine groups, polyallylamine as a ligand led to the production of branched nanostructures after seeded growth (Figure S11). However, branching was not extensive due to the limited capability of the linear ligands to regulate the surface strain.

Further investigation of the crystal structures between an island and its mother seed by high-resolution transmission electron microscopy (HRTEM) indicates the existence of many crystal twins and defects within the islands (Figures 3d and S12). To quantify the displacement and strain fields in crystalline lattices at a nanoscale resolution, we employed

https://doi.org/10.1021/jacs.1c11242
J. Am. Chem. Soc. 2021, 143, 20513−20523

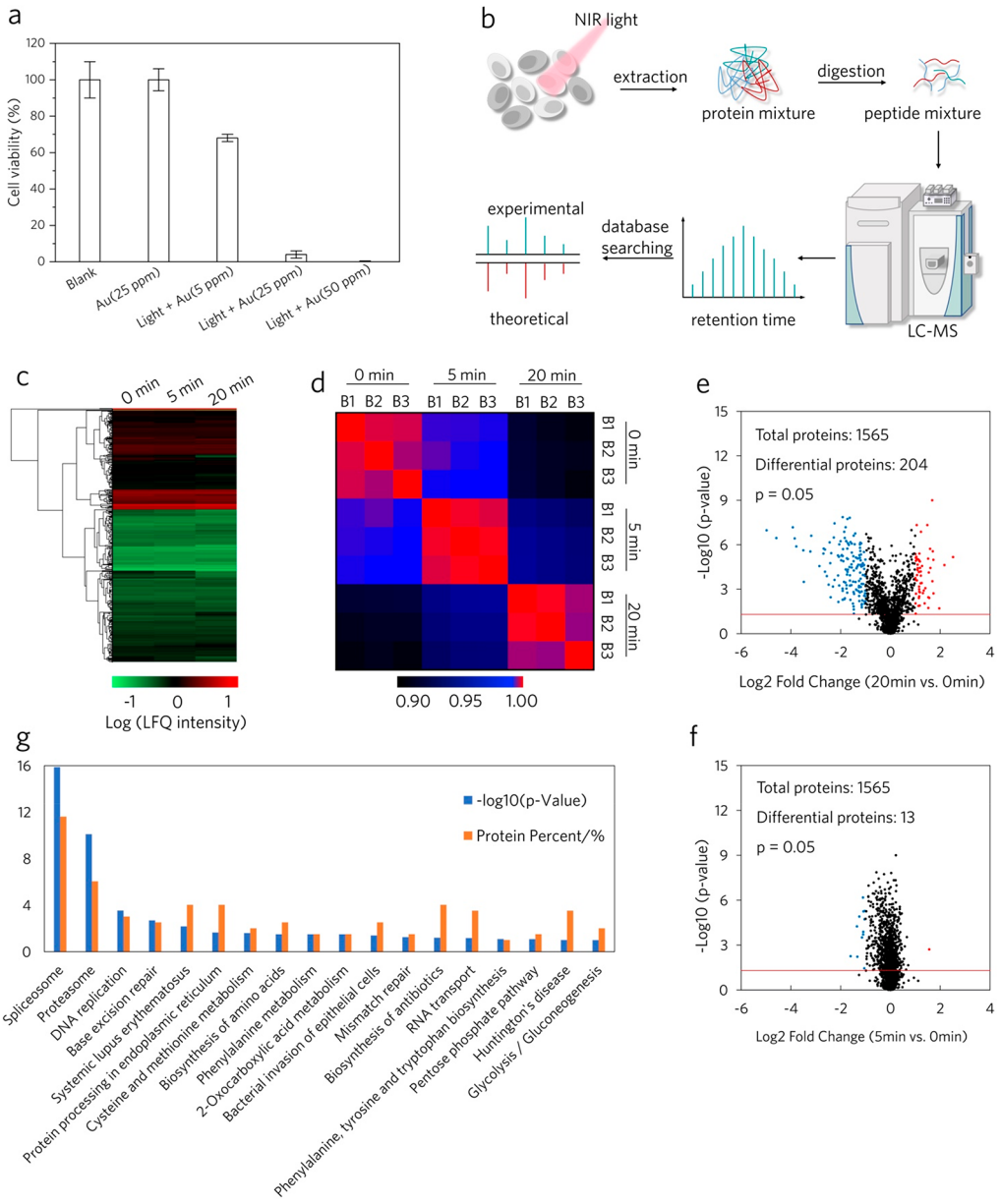

Figure 5. Proteomics analysis for photothermal therapy. (a) Effect of the concentration of Au on the photothermal therapeutic efficiency (0.5 W/cm^2 for 20 min). (b) Schematic illustration of the proteomics analysis of photothermal therapy by LC-MS. (c) Heatmap showing the expression levels of all the quantified proteins. The LFQ intensity of the identified proteins in each group was converted to log10 and normalized to between −1 and 1, reflecting the difference in protein expression levels under different conditions. (d) Cluster analysis of quantified proteins. (e and f) Volcano plots of proteins under perturbation. To draw the volcano graph, log2 values of the (5 min LFQ intensity)/(0 min LFQ intensity) ratio or log2 values of the (20 min)/(0 min) ratio was set as the *x*-axis and the −log10(*P*-value) was set as the *y*-axis. (g) KEGG of differential proteins (20 vs 0 min). DAVID Bioinformatics Resources 6.8 (https://david.ncifcrf.gov/) was used for the GO analysis of differential proteins.

geometric phase analysis (GPA) images (see part III in the Supporting Information).[41,42] Although the lattice strain in the HRTEM image cannot be clearly visualized by the naked eye, it has a significant contrast in the GPA image. A relatively large stress effect was observed inside the crystal (white arrow), proving that the epitaxial growth mode could not be maintained during the overgrowth process. Meanwhile, the considerable strain on the surface suggests its continuous accumulation due to the adsorption of polydopamine on the Au surface during overgrowth.

Photothermal Conversion. Consistent with our hypothesis, the as-prepared Au superparticles exhibit broadband absorption in the visible to NIR window even at a low concentration (Figure 4a). Following the Lambert−Beer law ($A/L = \varepsilon C$, where A is the absorption intensity, L the length of the cell, ε the extinction coefficient, and C is the concentration), a linear dependence of A/L on the concentration was obtained (Figure S13), and the extinction coefficient at 808 nm was measured at 7.9 L g^{-1} cm^{-1}, which is smaller than that of conventional Au nanostructures (~15.0 L g^{-1} cm^{-1}). While a small extinction coefficient typically means an inefficient photothermal effect, the temperature elevation, in this case, is significant (Figure 4b). The PCE is as high as 91.0% (Figure 4c), which is much higher than those of other plasmonic photothermal agents. The seemingly contradictory

https://doi.org/10.1021/jacs.1c11242
J. Am. Chem. Soc. 2021, 143, 20513−20523

results imply that the extinct lights are converted to heat with a low scattering effect.

Since σ_{abs} is difficult to measure experimentally, we performed calculations based on finite-difference time-domain (FDTD) solutions with the help of the electron tomography-assisted true 3D reconstruction process. The σ_{abs} and σ_{sca} values of branched Au superparticles were calculated and validated by approximating spheres to cubes with a slight deviation (see part IV in the Supporting Information). As shown in Figure 4d, σ_{sca} is small and the absorption efficiency is beyond 95% in the NIR range, suggesting a high light absorption efficiency. The absorption of the Au superparticles is enhanced by the substantial plasmon coupling events and, more importantly, the multiple reflections and absorptions within the superparticles as enabled by their multibranched structures. The broadening of the absorption peak is ascribed to the probable multiple or high-order scattering effects, which are triggered by the multiple built-in hotspots inside the 3D structure. We focused on the absorption efficiency at around 808 nm, and the reconstructed nanostructure had an extremely high absorption efficiency of 97.04% at 810 nm. By plotting the electric field at 810 nm (Figure 4e), we found a substantial electric field enhancement, which should be attributed to the high absorption ability.

We also examined the polarization dependence of the light absorption of our branched Au superparticles. The nanostructure shows almost identical absorption profiles with different polarization directions, which indicates that our branched Au superparticles absorb laser energy regardless of the polarization direction of light. This unique behavior is consistent with our original design and also contributes to the high photothermal efficiency. Further, the branched Au superparticles were found to exhibit high thermal and light stability (Figure S14), making them ideal photothermal agents.

***In Vitro* Photothermal Therapy.** Photothermal therapy has attracted significant attention for cancer treatment due to its noninvasive nature, high specificity, and insignificant side effects.[43] Due to the excellent photothermal efficiency, branched Au superparticles were applied to kill cancer cells *in vitro*. The nanostructures were first functionalized with RGD oligopeptide (RGDRGDRGDRGDPGC) and polyethylene glycol thiol (PEG) to increase the biocompatibility and targeting to cell. The change of the surface charge from -34.1 ± 0.4 to $+11.7 \pm 0.2$ mV indicates the successful conjugation of the RGD peptides and PEG thiols. Since the SCMM-7721cells themselves have negligible absorption to NIR light, no obvious change of the cell viability could be found even with a laser power reaching 1 W/cm^2. In comparison, when the SCMM-7721cells were incubated with Au nanostructures (5 ppm) and then illuminated with a low-power light of 0.5 W/cm^2 for 20 min, the cell viability sharply decreased to 68% (Figure 5a). Most of the cells were killed by increasing the concentration of Au nanostructures to 25 ppm with the same irradiation conditions, demonstrating a high photothermal therapeutic effect. We thereby performed further experiments with a concentration of 25 ppm.

Proteomics Analysis for Photothermal Therapy. As one of the most important parameters, temperature influences almost all biological processes at the molecular and cellular levels.[44] For example, when the local temperature is raised to 40−60 °C, proteins aggregate and denaturize and the structures of organelles start to change, resulting in irreversible damage and finally cell apoptosis within 4−6 min. Moreover, hyperthermia within cancer fuci can induce the release of cancer antigens and proinflammatory cytokines to promote anticancer immunity that kills cancer cells synergistically, further demonstrating the high efficiency and potential of photothermal therapy for cancer treatment.

To gain a global view of proteome change during the photothermal therapy, we applied label-free quantitative proteomics to identify and quantify protein expression changes in SMMC-7721 cells after incubation with different stimulus conditions.[45,46] In this experiment, proteins were extracted and analyzed by liquid chromatography−mass spectrometry (LC-MS) (Figure 5b). The MS raw files were searched with Maxquant for label-free quantification (LFQ). In total, over 2000 proteins were identified in three biological replications, and about 1600 common proteins were quantified in three different treatment groups (Figure 5c; 0, 5, and 20 min). The correlation heat map was drawn by calculating the Pearson correlation coefficients between the LFQ intensities of different groups of proteins (Figures 5d and S15). The clustering analysis shows that the control group (0 min) and experimental groups were separately clustered, indicating the good reproducibility of the proteomics experiments. After log10 conversion of the proteome LFQ intensity data, Student's *t*-test analysis was performed, and the *P*-value threshold was set to 0.05 to select proteins with significant differences. Proteins with (5 min)/(0 min) ratios or (20 min)/(0 min) ratios more than 2 or less than 0.5 were considered differential proteins (Figure 5e and f). Compared with the control group, the differential analysis identified proteins with significant changes (Figure 5e) in photothermal-treated groups when the exposure time reached 20 min. However, when the exposure time was shortened to 5 min, the number of differential proteins was only 13, demonstrating almost no change at all (Figure 5f). The number of up- and down-regulated proteins in each group are shown in Figure S16a.

A comparison of differentially expressed proteins identified at different times can be found in the Venn diagram (Figure S16b). As shown in Figure 5g, differential proteins are distributed in different biological pathways. Pathway analysis revealed the perturbation of significant signaling pathways related to apoptosis, including spliceosome, proteasome, and glycolysis or gluconeogenesis. The regulation of apoptosis may act by affecting the energy and materials metabolism (Figure S17). Energy generation-related proteins PGM1 and ALDOA were found to be down-regulated in both the glycolysis or gluconeogenesis and pentose phosphate pathways, leading to decreased glycolysis and reduced ATP synthesis. Insufficient ATP energy then caused cell apoptosis.[47] For the materials metabolism part, the photothermal treatment down-regulated the expression of phenylalanine metabolism pathway-related proteins (GOT1L1MIF), resulting in an inhibition of phenylalanine metabolism. Elevated levels of phenylalanine are known to induce apoptosis.[48] In addition, the proteasome can remove some junk proteins and prevent cell apoptosis. The core particle of the proteasome was overall down-regulated, leading to the inactivation of the proteasome. These junk proteins cannot be removed after inactivation, and the cell function becomes disordered, leading to apoptosis or necrosis.[49] Therefore, the energy and material metabolism pathways were disturbed after the photothermal treatment, both of which caused tumor cell apoptosis.

https://doi.org/10.1021/jacs.1c11242
J. Am. Chem. Soc. 2021, 143, 20513−20523

CONCLUSION

In summary, we have developed a strain modulation strategy to control the seeded growth of highly branched 3D Au nanostructures. The redox reaction between dopamine and Au^{3+} ions plays a vital role in the *in situ* formation of polydopamine and its progressive deposition to the growing surface of Au nanostructures to prevent conformal coating and promote the continuous island growth of Au, producing highly branched 3D superstructures. Thanks to the negligible scattering cross-section, these branched Au nanostructures showed an extraordinary high photothermal performance with a recorded efficiency of 91.0%. When such nanostructures are used as photothermal agents to kill cancer cells, the light intensity and dosage requirements could be minimized to a very low level, holding great promises in clinical applications. The proposed unconventional seeded growth strategy is general and may be extended to the synthesis of 3D branched superstructures of other plasmonic metals such as copper and silver, producing efficient photothermal converters with broad applications in areas such as catalysis and solar energy harvesting.

EXPERIMENTAL SECTION

Chemicals. Hydrogen tetrachloroaurate (III) trihydrate ($HAuCl_4 \cdot 3H_2O$, 99.9%), L-ascorbic acid, polyvinylpyrrolidone (PVP, Mw = 10,000), potassium iodide (KI, 99%), sodium borohydride ($NaBH_4$, 99%), L-ascorbic acid (AA, 99%), polyethylene glycol thiol (Mw = 5000, PEG), formic acid (FA), trypsin (TPCK-treated), iodoacetamide (IAA), dithiothreitol (DTT), trifluoroacetic acid (TFA), acetonitrile (ACN), mammalian cell protease inhibitors, and urea were purchased from Sigma-Aldrich. Trisodium citrate dihydrate (TSC, 99%), dopamine (99%), Catechol (99%), and tris-(hydroxymethyl)methyl aminomethane (Tris, 99.9%) were purchased from Aladdin. Hydrochloric acid (HCl,) was purchased from Sinopharm Chemical Reagent Co., Ltd. All chemicals were used as received without further purification. Cell Counting Kit-8 (CCK-8) was purchased from Dojindo (Japan). Cell-penetrating peptide RGD (RGDRGDRGDRGDPGC) was purchased from Nanjing Jiepeptide Biological Co., Ltd. (China).

Synthesis of Au NPs (14 nm). Au NPs with a diameter of 14 nm were prepared by the one-step seed growth method. In step 1, small Au seeds were first prepared. To 9 mL of deionized (DI) water were added 0.5 mL $HAuCl_4$ (5 mM) and 0.5 mL TSC (5 mM). Then, $NaBH_4$ (0.3 mL, 0.1M) was quickly injected into the mixture under vigorous stirring, leading to solution color to change to yellowish-red immediately. After 4 h, the solution was stored at 4 °C for subsequent seeded growth. In step 2, KI (1 mL, 0.2 M), PVP (2.5 mL, 5 wt %), $HAuCl_4$ (1.25 mL, 25.4 mM), and AA (1.25 mL, 0.1 M) were mixed with 7.3 mL of DI water. Then, 3 mL of the Au seed solution was quickly injected into the solution under vigorous stirring. The final product was collected by centrifugation after 10 min and redispersed in 52 mL of DI water.

Synthesis of Au NPs. In 9 mL of a Tris-HCl buffer solution under nitrogen flow was dispersed 100 μL of Au NPs (14 nm). Then, dopamine (50 μL, 4 mg/mL) and $HAuCl_4$ (100 μL, 25.4 mM) were added to the buffer solution sequentially. Immediately, the color changed to orange from light pink and slowly turned to black after 1 h. The Au NPs were collected by centrifugation and redispersed in DI water after 6 h.

Surface Modification. First, 1 mL of Au nanostructures (0.68 mg/mL) and 330 μL of the RGD peptide (2 mg/mL) were mixed and reacted at 4 °C for 12 h. Then, the mixture was centrifuged to remove the supernatant, and the product was dispersed to 1 mL of H_2O. Finally, 330 μL of polyethylene glycol thiol (2 mg/mL, Mw = 5000) was added to the mixture. The mixture was centrifuged to remove the supernatant, and the product was dispersed to 0.68 mL of H_2O.

Cell Viability Assay. The cell viability was assessed by the CCK8 kit. The SMMC-7721 cells were cultured in a DMEM medium containing 10% FBS and 1% PBS in a humidified incubator of 5% CO_2 and 95% air at 37 °C. Cells were seeded on 96-well plates for 24 h, and PBS was added into wells as the control group. Different concentrations of Au were added into wells as the experimental group, and the wells were incubated for 24 h. After CW laser irradiation (808 nm 0.5 W/cm^2), CCK8 was added into the wells, and the mixtures were incubated for 3 h. The optical density was measured on a microplate reader at 450 nm. The cell viability was calculated through the following equations: cell viability (%) = 100% × (OD of T-OD of B1)/(OD of C-OD of B2), in which "OD of T" is the optical density of the test experimental group, "OD of C" is the optical density of the test control group, "OD of B1" is the optical density of the blank experimental group, and "OD of B2" is the optical density of the blank control group. The results are the average of five biological replicates.

Photothermal Therapy and Protein Sample Preparation. The SMMC-7721 cells were cultured in a DMEM medium containing 10% FBS and 1% PBS in a humidified incubator of 5% CO_2 and 95% air at 37 °C. SMMC-7721 cells were incubated overnight with 5 μM Au in complete media and then exposed to a CW laser (808 nm 0.5 W/cm^2) for different durations. All cells reaching 80% confluence were detached with 0.25% trypsin/EDTA and centrifuged (500 rpm, 5 min) for collection. Cells were washed three times with cold PBS and suspended in lysis buffer (8 M urea, 10 mM PBS, and 1% (v/v) protease inhibitor cocktail). After ultrasonication for 120 s (5 s intervals every 5 s) in an ice bath, insoluble portions were separated from the soluble ones by centrifugation at 16 000 × g for 30 min at 4 °C. Protein concentrations were determined using a BCA assay. After being treated with DTT and IAA, the proteins were purified by a MWCO 10 kd membrane. Afterward, the proteins were digested with a substrate-to-enzyme ratio of 25:1 (m/m) at 37 °C for 12 h

NanoRPLC-ESI-MS/MS Methods. For the SMMC-7721 digest analysis, the mixture was automatically loaded onto an RP trap column (150 μm i.d. × 5 cm) and separated by a C18 capillary column (150 μm i.d. × 15 cm). The trap column and the analytical column were both packed in-house with 5 μm and 100 Å Venusil XBP C18 silica particles. In order to study the peptides, two mobile phases (A, 2% (v/v) ACN with 0.1% (v/v) FA and B, 98% (v/v) ACN with 0.1% (v/v) FA) were used to generate an 85 min gradient with the flow rate of 600 nL/min (50 min from 7% to 23% B, 20 min from 23% to 40% B, 2 min from 40% to 80% B, and 13 min kept at 80% B). A Q-Exactive mass spectrometer (Thermo-Fisher, San Jose, CA) was operated in full scan (70000 fwhm, 350−1800 m/z) and product scan (17500 fwhm, 100−1000 m/z) modes at the positive ion mode. The electro-spray voltage was 2.3 kV, and the heated capillary temperature was 270 °C. All the mass spectra were recorded with Xcalibur software (ver. 3.1, Thermo Fisher Scientific). MS/MS spectra were acquired in the data-dependent acquisition mode, and the 20 most intense peaks with a charge state ≥2 were selected for sequencing in the HCD collision cell with a stepped collision energy of 28%, 30%, and 32%.

MS Data Analysis. Maxquant 1.6.5.0 was applied for the database search against the swissprot Human fasta database (downloaded on April 4, 2019). The corresponding reversed database was also used to evaluate the false discovery rate (FDR) of peptide identification in the database searching process. The parameters of the database search include up to three missed cleavages that allowed for full tryptic digestion, a precursor ion mass tolerance of 10 ppm, a product ion mass tolerance of 20 mmu, carbamidomethylation (C) as a fixed modification, and oxidation (M) and acetyl (protein N-term) as variable modifications. Peptide spectral matches (PSM) were validated using a perculator based on a q-value at a 1% false discovery rate (FDR). The MaxLFQ algorithm integrated within MaxQuant (ver. 1.6.5.0) was used for the label-free quantification (LFQ) analysis of proteins with default parameters.

Characterization. UV−vis−NIR absorbance spectra were recorded in a range of 400−900 nm using a spectrometer (Maya 2000 Pro, Ocean Optics). TEM, HRTEM, HAADF-STEM, and elemental mapping images were acquired by field emission high-resolution

https://doi.org/10.1021/jacs.1c11242
J. Am. Chem. Soc. 2021, 143, 20513−20523

transmission electron microscopy (FEI Talos F200X, Thermo Fisher). The photographs were taken by using a Canon 80D SLR camera. The ζ-potential was measured using the Nano-ZS90 zetasizer (Malvern, UK).

■ ASSOCIATED CONTENT

Supporting Information

The Supporting Information is available free of charge at https://pubs.acs.org/doi/10.1021/jacs.1c11242.

Electron tomography of one typical Au (AVI)

Electron tomography of one typical Au after reconstructing the obtained pictures (AVI)

Electron tomography of one typical Au after slicing the obtained pictures (AVI)

Simulations, theory of GPA, TEM images of samples, photothermal stability, and proteomics analysis (PDF)

■ AUTHOR INFORMATION

Corresponding Authors

Bo Jiang − *Department of Chemistry, University of California, Riverside, California 92521, United States; CAS Key Laboratory of Separation Science for Analytical Chemistry, National Chromatographic Research and Analysis Center, Dalian Institute of Chemical Physics, Chinese Academy of Science, Dalian, Liaoning 116023, P.R. China;* orcid.org/0000-0001-5647-6890; Email: jiangbo@dicp.ac.cn

Jinxing Chen − *Institute of Functional Nano & Soft Materials (FUNSOM), Jiangsu Key Laboratory for Carbon-Based Functional Materials and Devices, and Joint International Research Laboratory of Carbon-Based Functional Materials and Devices, Soochow University, Suzhou, Jiangsu 215123, P.R. China;* orcid.org/0000-0001-9254-7430; Email: chenjinxing@suda.edu.cn

Yadong Yin − *Department of Chemistry, University of California, Riverside, California 92521, United States;* orcid.org/0000-0003-0218-3042; Email: yadong.yin@ucr.edu

Authors

Qixuan Zhong − *Institute of Functional Nano & Soft Materials (FUNSOM), Jiangsu Key Laboratory for Carbon-Based Functional Materials and Devices, and Joint International Research Laboratory of Carbon-Based Functional Materials and Devices, Soochow University, Suzhou, Jiangsu 215123, P.R. China*

Ji Feng − *Department of Chemistry, University of California, Riverside, California 92521, United States*

Yulong Fan − *Department of Materials Science and Engineering, City University of Hong Kong, Kowloon, Hong Kong 999077, P.R. China;* orcid.org/0000-0001-8610-2072

Qiao Zhang − *Institute of Functional Nano & Soft Materials (FUNSOM), Jiangsu Key Laboratory for Carbon-Based Functional Materials and Devices, and Joint International Research Laboratory of Carbon-Based Functional Materials and Devices, Soochow University, Suzhou, Jiangsu 215123, P.R. China;* orcid.org/0000-0001-9682-3295

Complete contact information is available at: https://pubs.acs.org/10.1021/jacs.1c11242

Notes

The authors declare no competing financial interest.

■ ACKNOWLEDGMENTS

This work was supported in part by the National Natural Science Foundation of China (51901147, J.C.; 51922073, Q.Z.), the Natural Science Foundation of Jiangsu Province (BK20180097, Q.Z.), and the Engineering Research Centers Program of the U.S. National Science Foundation under NSF Cooperative Agreement no. 1941543 (Y.Y.). J.C. and Q.Z. acknowledge the financial support from the Suzhou Key Laboratory of Functional Nano and Soft Materials, Collaborative Innovation Center of Suzhou Nano Science and Technology, and the 111 Project. The authors thank Dr. Fan Yang (Iowa State University), He Wang (Dalian Institute of Chemical Physics, CAS), Prof. Lihua Zhang (Dalian Institute of Chemical Physics, CAS), Dr. Wenxiu Yang (Southeast University), Dr. Muhan Cao (Soochow University), and Dr. Bin Song (Soochow University) for their help with discussion and characterizations. The authors also thank J. J. P. Peters for the release of the Strain++ software.

■ ABBREVIATIONS

(PCE), photothermal conversion efficiencies; GPA, geometric phase analysis; EDS, energy-dispersive X-ray spectrometry; HRTEM, high-resolution transmission electron microscopy; FDTD, finite-difference time-domain; PEG, polyethylene glycol thiol; LC-MS, liquid chromatography−mass spectrometry; LFQ, label-free quantification

■ REFERENCES

(1) Liu, D.; Zhou, F.; Li, C.; Zhang, T.; Zhang, H.; Cai, W.; Li, Y. Black Gold: Plasmonic Colloidosomes with Broadband Absorption Self-Assembled from Monodispersed Gold Nanospheres by Using a Reverse Emulsion System. *Angew. Chem., Int. Ed.* **2015**, *54* (33), 9596−9600.

(2) Kwon, N.; Oh, H.; Kim, R.; Sinha, A.; Kim, J.; Shin, J.; Chon, J. W. M.; Lim, B. Direct Chemical Synthesis of Plasmonic Black Colloidal Gold Superparticles with Broadband Absorption Properties. *Nano Lett.* **2018**, *18* (9), 5927−5932.

(3) Chen, J.; Ye, Z.; Yang, F.; Yin, Y. Plasmonic Nanostructures for Photothermal Conversion. *Small Sci.* **2021**, *1* (2), 2000055.

(4) Huang, J.; Liu, C.; Zhu, Y.; Masala, S.; Alarousu, E.; Han, Y.; Fratalocchi, A. Harnessing structural darkness in the visible and infrared wavelengths for a new source of light. *Nat. Nanotechnol.* **2016**, *11* (1), 60−66.

(5) Bae, K.; Kang, G.; Cho, S. K.; Park, W.; Kim, K.; Padilla, W. J. Flexible thin-film black gold membranes with ultrabroadband plasmonic nanofocusing for efficient solar vapour generation. *Nat. Commun.* **2015**, *6*, 10103.

(6) Abdelaziz, R.; Disci-Zayed, D.; Hedayati, M. K.; Pohls, J. H.; Zillohu, A. U.; Erkartal, B.; Chakravadhanula, V. S.; Duppel, V.; Kienle, L.; Elbahri, M. Green chemistry and nanofabrication in a levitated Leidenfrost drop. *Nat. Commun.* **2013**, *4*, 2400.

(7) Zhou, J.; Jiang, Y.; Hou, S.; Upputuri, P. K.; Wu, D.; Li, J.; Wang, P.; Zhen, X.; Pramanik, M.; Pu, K.; Duan, H. Compact Plasmonic Blackbody for Cancer Theranosis in the Near-Infrared II Window. *ACS Nano* **2018**, *12* (3), 2643−2651.

(8) Huang, P.; Lin, J.; Li, W.; Rong, P.; Wang, Z.; Wang, S.; Wang, X.; Sun, X.; Aronova, M.; Niu, G.; Leapman, R. D.; Nie, Z.; Chen, X. Biodegradable gold nanovesicles with an ultrastrong plasmonic coupling effect for photoacoustic imaging and photothermal therapy. *Angew. Chem., Int. Ed.* **2013**, *52* (52), 13958−13964.

(9) Liu, Y.; Yang, X.; Huang, Z.; Huang, P.; Zhang, Y.; Deng, L.; Wang, Z.; Zhou, Z.; Liu, Y.; Kalish, H.; Khachab, N. M.; Chen, X.; Nie, Z. Magneto-Plasmonic Janus Vesicles for Magnetic Field-Enhanced Photoacoustic and Magnetic Resonance Imaging of Tumors. *Angew. Chem., Int. Ed.* **2016**, *55* (49), 15297−15300.

(10) Xu, H.; Alvaro, P.; Xiang, Y.; Kelly, T. S.; Ren, Y.-X.; Zhang, C.; Chen, Z. Plasmonic resonant nonlinearity and synthetic optical properties in gold nanorod suspensions. *Photonics Res.* **2019**, *7* (1), 28−35.
(11) Clark, B. D.; Jacobson, C. R.; Lou, M.; Yang, J.; Zhou, L.; Gottheim, S.; DeSantis, C. J.; Nordlander, P.; Halas, N. J. Aluminum Nanorods. *Nano Lett.* **2018**, *18* (2), 1234−1240.
(12) Zhou, L.; Tan, Y.; Wang, J.; Xu, W.; Yuan, Y.; Cai, W.; Zhu, S.; Zhu, J. 3D self-assembly of aluminium nanoparticles for plasmon-enhanced solar desalination. *Nat. Photonics* **2016**, *10* (6), 393−398.
(13) Chen, J.; Feng, J.; Li, Z.; Xu, P.; Wang, X.; Yin, W.; Wang, M.; Ge, X.; Yin, Y. Space-Confined Seeded Growth of Black Silver Nanostructures for Solar Steam Generation. *Nano Lett.* **2019**, *19* (1), 400−407.
(14) De Aberasturi, D. J.; Serrano-Montes, A. B.; Liz-Marzán, L. M. Modern Applications of Plasmonic Nanoparticles: From Energy to Health. *Adv. Opt. Mater.* **2015**, *3* (5), 602−617.
(15) Jain, P. K.; El-Sayed, I. H.; El-Sayed, M. A. Au nanoparticles target cancer. *Nano Today* **2007**, *2* (1), 18−29.
(16) Kim, H. S.; Lee, D. Y. Near-Infrared-Responsive Cancer Photothermal and Photodynamic Therapy Using Gold Nanoparticles. *Polymers* **2018**, *10* (9), 961.
(17) Chen, H.; Shao, L.; Ming, T.; Sun, Z.; Zhao, C.; Yang, B.; Wang, J. Understanding the photothermal conversion efficiency of gold nanocrystals. *Small* **2010**, *6* (20), 2272−2280.
(18) Zheng, T.; Li, G. G.; Zhou, F.; Wu, R.; Zhu, J. J.; Wang, H. Gold-Nanosponge-Based Multistimuli-Responsive Drug Vehicles for Targeted Chemo-Photothermal Therapy. *Adv. Mater.* **2016**, *28* (37), 8218−8226.
(19) Liu, K.; Bai, Y.; Zhang, L.; Yang, Z.; Fan, Q.; Zheng, H.; Yin, Y.; Gao, C. Porous Au-Ag Nanospheres with High-Density and Highly Accessible Hotspots for SERS Analysis. *Nano Lett.* **2016**, *16* (6), 3675−3681.
(20) Chen, Y.; Wang, Z.; He, Y.; Yoon, Y. J.; Jung, J.; Zhang, G.; Lin, Z. Light-enabled reversible self-assembly and tunable optical properties of stable hairy nanoparticles. *Proc. Natl. Acad. Sci. U. S. A.* **2018**, *115* (7), E1391−E1400.
(21) Liu, Y.; Wang, J.; Zhang, M.; Li, H.; Lin, Z. Polymer-Ligated Nanocrystals Enabled by Nonlinear Block Copolymer Nanoreactors: Synthesis, Properties, and Applications. *ACS Nano* **2020**, *14* (10), 12491−12521.
(22) Chen, Y.; Yang, D.; Yoon, Y. J.; Pang, X.; Wang, Z.; Jung, J.; He, Y.; Harn, Y. W.; He, M.; Zhang, S.; Zhang, G.; Lin, Z. Hairy Uniform Permanently Ligated Hollow Nanoparticles with Precise Dimension Control and Tunable Optical Properties. *J. Am. Chem. Soc.* **2017**, *139* (37), 12956−12967.
(23) Jia, J.; Liu, G.; Xu, W.; Tian, X.; Li, S.; Han, F.; Feng, Y.; Dong, X.; Chen, H. Fine-Tuning the Homometallic Interface of Au-on-Au Nanorods and Their Photothermal Therapy in the NIR-II Window. *Angew. Chem.* **2020**, *132* (34), 14551−14556.
(24) Chen, G.; Gibson, K. J.; Liu, D.; Rees, H. C.; Lee, J. H.; Xia, W.; Lin, R.; Xin, H. L.; Gang, O.; Weizmann, Y. Regioselective surface encoding of nanoparticles for programmable self-assembly. *Nat. Mater.* **2019**, *18* (2), 169−174.
(25) Prieto, J. E.; Markov, I. Thermodynamic driving force of formation of coherent three-dimensional islands in Stranski-Krastanov growth. *Phys. Rev. B: Condens. Matter Mater. Phys.* **2002**, *66* (7), 073408.
(26) Bauer, E.; van der Merwe, J. H. Structure and growth of crystalline superlattices: From monolayer to superlattice. *Phys. Rev. B: Condens. Matter Mater. Phys.* **1986**, *33* (6), 3657−3671.
(27) Wang, G.; Liu, Y.; Gao, C.; Guo, L.; Chi, M.; Ijiro, K.; Maeda, M.; Yin, Y. Island Growth in the Seed-Mediated Overgrowth of Monometallic Colloidal Nanostructures. *Chem* **2017**, *3* (4), 678−690.
(28) Huang, J.; Zhu, Y.; Liu, C.; Shi, Z.; Fratalocchi, A.; Han, Y. Unravelling Thiol's Role in Directing Asymmetric Growth of Au Nanorod-Au Nanoparticle Dimers. *Nano Lett.* **2016**, *16* (1), 617−623.
(29) Feng, J.; Xu, D.; Yang, F.; Chen, J.; Wu, C.; Yin, Y. Surface Engineering and Controlled Ripening for Seed-Mediated Growth of Au Islands on Au Nanocrystals. *Angew. Chem. Int. Ed.* **2021**, *60* (31), 16958−16964.
(30) Kwon, S. G.; Krylova, G.; Phillips, P. J.; Klie, R. F.; Chattopadhyay, S.; Shibata, T.; Bunel, E. E.; Liu, Y.; Prakapenka, V. B.; Lee, B.; Shevchenko, E. V. Heterogeneous nucleation and shape transformation of multicomponent metallic nanostructures. *Nat. Mater.* **2015**, *14* (2), 215−223.
(31) Day, H. A.; Bartczak, D.; Fairbairn, N.; McGuire, E.; Ardakani, M.; Porter, A. E.; Kanaras, A. G. Controlling the three-dimensional morphology of nanocrystals. *CrystEngComm* **2010**, *12*, 4312.
(32) Downey, J. S.; Frank, R. S.; Li, W.-H.; Stöver, H. D. H. Growth Mechanism of Poly(divinylbenzene) Microspheres in Precipitation Polymerization. *Macromolecules* **1999**, *32* (9), 2838−2844.
(33) Zhou, J.; Wang, P.; Wang, C.; Goh, Y. T.; Fang, Z.; Messersmith, P. B.; Duan, H. Versatile Core-Shell Nanoparticle@Metal-Organic Framework Nanohybrids: Exploiting Mussel-Inspired Polydopamine for Tailored Structural Integration. *ACS Nano* **2015**, *9* (7), 6951−6960.
(34) Hou, S.; Chen, Y.; Lu, D.; Xiong, Q.; Lim, Y.; Duan, H. A Self-Assembled Plasmonic Substrate for Enhanced Fluorescence Resonance Energy Transfer. *Adv. Mater.* **2020**, *32* (8), 1906475.
(35) Zhou, J.; Xiong, Q.; Ma, J.; Ren, J.; Messersmith, P. B.; Chen, P.; Duan, H. Polydopamine-Enabled Approach toward Tailored Plasmonic Nanogapped Nanoparticles: From Nanogap Engineering to Multifunctionality. *ACS Nano* **2016**, *10* (12), 11066−11075.
(36) Yin, Y.; Alivisatos, A. P. Colloidal nanocrystal synthesis and the organic-inorganic interface. *Nature* **2005**, *437* (7059), 664−670.
(37) Liebscher, J.; Mrowczynski, R.; Scheidt, H. A.; Filip, C.; Hadade, N. D.; Turcu, R.; Bende, A.; Beck, S. Structure of polydopamine: a never-ending story? *Langmuir* **2013**, *29* (33), 10539−10548.
(38) Lynge, M. E.; van der Westen, R.; Postma, A.; Stadler, B. Polydopamine–a nature-inspired polymer coating for biomedical science. *Nanoscale* **2011**, *3* (12), 4916−4928.
(39) Chen, J.; Bai, Y.; Feng, J.; Yang, F.; Xu, P.; Wang, Z.; Zhang, Q.; Yin, Y. Anisotropic Seeded Growth of Ag Nanoplates Confined in Shape-Deformable Spaces. *Angew. Chem. Int. Ed.* **2021**, *133* (8), 4163−4170.
(40) Chen, J.; Feng, J.; Yang, F.; Aleisa, R.; Zhang, Q.; Yin, Y. Space-Confined Seeded Growth of Cu Nanorods with Strong Surface Plasmon Resonance for Photothermal Actuation. *Angew. Chem. Int. Ed.* **2019**, *131* (27), 9376−9382.
(41) Hÿtch, M. J.; Snoeck, E.; Kilaas, R. Quantitative measurement of displacement and strain fields from HREM micrographs. *Ultramicroscopy* **1998**, *74* (3), 131−146.
(42) Oh, M. H.; Cho, M. G.; Chung, D. Y.; Park, I.; Kwon, Y. P.; Ophus, C.; Kim, D.; Kim, M. G.; Jeong, B.; Gu, X. W.; Jo, J.; Yoo, J. M.; Hong, J.; McMains, S.; Kang, K.; Sung, Y. E.; Alivisatos, A. P.; Hyeon, T. Design and synthesis of multigrain nanocrystals via geometric misfit strain. *Nature* **2020**, *577* (7790), 359−363.
(43) Chu, K. F.; Dupuy, D. E. Thermal ablation of tumours: biological mechanisms and advances in therapy. *Nat. Rev. Cancer* **2014**, *14* (3), 199−208.
(44) Nam, J.; Son, S.; Ochyl, L. J.; Kuai, R.; Schwendeman, A.; Moon, J. J. Chemo-photothermal therapy combination elicits anti-tumor immunity against advanced metastatic cancer. *Nat. Commun.* **2018**, *9* (1), 1074.
(45) Slavov, N. Unpicking the proteome in single cells. *Science* **2020**, *367* (6477), 512−513.
(46) Liu, Y.; Beyer, A.; Aebersold, R. On the Dependency of Cellular Protein Levels on mRNA Abundance. *Cell* **2016**, *165* (3), 535−550.
(47) Ali, M. R.; Rahman, M. A.; Wu, Y.; Han, T.; Peng, X.; Mackey, M. A.; Wang, D.; Shin, H. J.; Chen, Z. G.; Xiao, H.; Wu, R.; Tang, Y.; Shin, D. M.; El-Sayed, M. A. Efficacy, long-term toxicity, and mechanistic studies of gold nanorods photothermal therapy of cancer in xenograft mice. *Proc. Natl. Acad. Sci. U. S. A.* **2017**, *114* (15), E3110−E3118.

https://doi.org/10.1021/jacs.1c11242
J. Am. Chem. Soc. 2021, 143, 20513−20523

(48) Ali, M. R.; Wu, Y.; Han, T.; Zang, X.; Xiao, H.; Tang, Y.; Wu, R.; Fernandez, F. M.; El-Sayed, M. A. Simultaneous Time-Dependent Surface-Enhanced Raman Spectroscopy, Metabolomics, and Proteomics Reveal Cancer Cell Death Mechanisms Associated with Gold Nanorod Photothermal Therapy. *J. Am. Chem. Soc.* **2016**, *138* (47), 15434−15442.
(49) Vlahakis, S. R.; Badley, A. D. Influence of proteasome inhibitors on apoptosis. *Curr. Opin. Clin. Nutr. Metab. Care* **2006**, *9* (1), 42−47.

https://doi.org/10.1021/jacs.1c11242
J. Am. Chem. Soc. 2021, 143, 20513−20523